Bridged structures in Ultrathin 2D materials for high toughness.

Kamalendu Paul[†§], Changjun Zhang[∥], Chi-Hua Yu[∥], Zhao Qin[†‡∞]*

[†]Laboratory for Multiscale Material Modelling, Syracuse University, 151L Link Hall, Syracuse University, Syracuse, NY 13244, USA

[‡]Department of Civil and Environmental Engineering, Syracuse University, 151L Link Hall, Syracuse University, Syracuse, NY 13244, USA

[§] Department of Physics, Syracuse University, 151L Link Hall, Syracuse University, Syracuse, NY 13244, USA

[∥] Department of Engineering Science, National Cheng Kung University, No.1, University Road, Tainan City 701, Taiwan

[∞] The BioInspired Institute, Syracuse University, NY 13244, USA

Corresponding Author, Zhao Qin, *E-mail: zqin02@syr.edu

KEYWORDS: Graphene, MoS_2, MXene, defects, energy dissipation, bridged structure

Abstract

2D materials such as graphene, monolayer MoS_2 and MXene are highly functional for their unique mechanical, thermal and electrical features and are considered building blocks for future ultrathin, flexible electronics. However, they can easily fracture from flaws or defects and thus it is important to increase their toughness in applications. Here, inspired by natural layered composites and architected 3D printed materials of high toughness, we introduce architected defects to the 2D materials and study their fracture in molecular dynamics simulations. We find that the length of the defects in the shape of parallel bridges is crucial to fracture toughness, as long bridges can significantly increase the toughness of graphene and MoS_2 but decrease the toughness of MXene, while short bridges show opposite effects. This strategy can increase the toughness of 2D materials without introducing foreign materials or altering the chemistry of the materials, providing a general method to improve their mechanics.

1. Introduction

Graphene, MoS_2, and MXene are interesting ultrathin 2D materials due to their incredible mechanical strength, electrical and thermal conductivity. A polycrystalline graphene is electrically conductive [1,2], has a Young's modulus of 1 TPa, a high ultimate mechanical strength of 90 GPa[3] and thermal conductivity of 5300 $W \cdot m^{-1} \cdot K^{-1}$ [4]. Graphene is used effectively under several extreme mechanical, electrical and thermal conditions with good performance, including battery, sensor, transistor and strong composites [5–7]. Monolayer MoS_2 (MoS_2 as an abbreviation) is a potential candidate for devising semiconductors due to its band gap of 1.8 eV [8,9]. This has led to applications in bendable wearable electronics. MoS_2 has been shown to have a Young's modulus of 270 GPa [8], an ultimate mechanical strength of almost 9.1 GPa[10] and a thermal conductivity of 34.5 $W \cdot m^{-1} \cdot K^{-1}$ [11]. MXene (as monolayer Ti_3C_2) has been discovered more recently than the other two materials [12] and is actively explored as candidates in energy storage, nanoelectronics and environmental applications due to its mechanical and chemical properties. MXene is reported to be electrically conductive [13], has a Young modulus of 473 GPa[14], a maximum mechanical strength of about 10 GPa[15] and a thermal conductivity of 55.8 $W \cdot m^{-1} \cdot K^{-1}$ [16,17].

These materials are ultrathin and thus a higher ultimate mechanical strength is crucial for its reliable applications. Doping methods and material composites to increase the mechanical strength of these materials have been an active area of research, while the mechanical enhancement is coupled with a change in electric properties. For example, doping MoS_2 with Ga^+ point defects can increase the strain energy release rate by 15% [18], doping MXene with Nb shows an increase in the band gap from 0.9 eV to 0.1 eV [19] and sequential bridging of hydrogen and covalent bonding agents is shown to increase its mechanical strength with 95% increase[20]. Introduction of CNT rebars embedded in graphene shows fourfold increase in fracture energy [21]. Reinforcing with rebar can locally increase the thickness of the material and reduce its flexibility, while chemical doping can significantly modify its electrical properties. On the other hand, ordered defects in graphene have been shown to be effective in tuning its mechanics without introducing foreign materials [22–24].

Here, we focus on architected defects in these materials in the form of bridges. Previous studies, in the continuum limit, have shown that pillared structures are effective in tuning the ductility and

toughness of 3D-printed samples [25]. It was shown that slender structures were able to have better strength because of better sharing of load among the pillars on the macroscale. It is not clear how this strategy can be applicable to different 2D materials and how the bridge defects interplay with the material fracture on the atomistic scale [14,26]. We create pristine graphene, MoS_2 and MXene samples with rectangular shaped defects and explore the strength by changing the height of these defects. To our knowledge, no such comparative study has been done.

2. Materials and Method

We simulated uniaxial strain in these architected 2D ultrathin samples. A schematic of the sample is shown in Fig. 1(a). Our typical sample is a piece of rectangular 2D material with a pre-existing sharp crack from one end and a periodic bridge-gap architecture in front of the crack. The height of the bridges varied from $h = 0$ Å referring to the pristine sample to h = 120 Å for the sample with the largest bridge height. The details of the fabricating the architecture is given in section 2.2. We use an adaptive intermolecular REBO potential (AIREBO)[27] for graphene and MoS_2[26] and a modified embedded atom method (MEAM) potential for MXene[28]. The details of the potentials used are discussed in section 2.1 .We studied the stress-strain profile, the virial stress, and the dissipation energy[29,30] of the samples. We also developed a simple mathematical theory to explain the dissipation energy using contributions from deformation energy and surface crack creation.

2.1 Molecular Modelling Potential

2.1.1 Graphene

The adaptive intermolecular REBO potential (AIREBO) [27] is used in this study for graphene sheet. The total potential energy, E_{CC}, capturing the interactions between the carbon atoms is given by

$$E_{CC} = \frac{1}{2}\sum_{i}\sum_{j\neq i}\left[E_{ij}^{REBO-CC} + E_{ij}^{LJ-CC} + \sum_{k\neq i,j}\sum_{l\neq i,j,k} E_{kijl}^{TORSION-CC}\right] \quad (1)$$

where $E_{ij}^{REBO-CC}$ and $E_{kijl}^{TORSION-CC}$ are the REBO term of hydrocarbon and TORSION term for four-body potential describing various dihedral angle preferences in hydrocarbon configurations respectively. The detailed expression and parameters of REBO and TORSION terms are given in the original paper of this force fields [27,31]. The long-range interaction among the atoms is given by the Lennard-Jones potential E_{ij}^{LJ-CC} with a cutoff of 8.5 Å. This potential can very well characterize the elastic mechanics of carbon allotropes except the non-physical stiffening of the stress-strain curve before bond rupture [32–34] because of the switching function. Thus, both radius cutoffs of the switching function in the AIREBO potential are set to 2.0 Å[35] to remove the effect of the switching function in the REBO potential as previous studies suggested [36,37].

2.1.2 MoS_2

We use REBO potential develop for MoS2 against Density Functional Theory (DFT) calculations as in the former work[26], since the original FF was not tuned for the failure of MoS2 system[38]. This potential was obtained by comparing the stress-strain curves and failure strain in the armchair and zigzag directions from DFT calculations. The total energy between the different sets of atoms is given by $E_{\mathrm{MoS_2}} = E_{Mo-Mo} + E_{Mo-S} + E_{S-S}$, where each individual energy term is of the form $E_{\alpha\beta}$

$$E_{\alpha\beta} = \frac{1}{2}\sum_{i}\sum_{j\neq i}\left[E_{ij}^{REBO-\alpha\beta} + E_{ij}^{LJ-\alpha\beta} + \sum_{k\neq i,j}\sum_{l\neq i,j,k} E_{kijl}^{TORSION-\alpha\beta}\right] \quad (2)$$

where α and β are a combination of Mo and S. The $E_{ij}^{REBO-\alpha\beta}$, $E_{ij}^{LJ-\alpha\beta}$and $E_{kijl}^{TORSION-\alpha\beta}$ are the REBO, Lennard-Jones and TORSION terms in the equation. There are three sets of combinations such as Mo-Mo, Mo-S and S-S. The parameters for the cutoff in the REBO terms were chosen to reduce the artificial stiffening effects caused by the switching function [26].

2.1.3 MXene (Ti_3C_2)

The interatomic interaction of MXene is defined based on the Modified Embedded-Atom Method (MEAM) interatomic potential of Ti-C bulk material[28]. The total energy is of the form given by E_{TiC}

$$E_{TiC} = \sum_{i}\left[F_i(\rho_i) + \frac{1}{2}\sum_{j\neq i} S_{ij}\,\phi_{ij}(R_{ij})\right] \quad (3)$$

where F_i is the embedding function of an atom *i* in a background electron density ρ_i, S_{ij} is the screening function and $\phi_{ij}(R_{ij})$ is the pair potential between atoms *i* and neighbors *j* as a function of the distance R_{ij} between the pairs. Since 2D MXene can stay alone, and the upper and lower surfaces do not tend to spontaneously form bonds in the thickness dimension, we simply tune the MEAM potential by reducing the radial cut-off distance from 4.6 Å to 3.95 Å. We also modified the effect of screening parameter denoted by $C_{min}(i-k-j)$ which determines the extent of screening of atom *k* on the interaction between two neighboring atoms *i* and *j*. We increase C_{min}(Ti–Ti–C), C_{min}(C–C–Ti) from 0.64 to 0.94 Å and decrease the screening parameters C_{min}(Ti–C–Ti), C_{min}(Ti–C–C), C_{min}(C–Ti–Ti), C_{min}(C–Ti–C) from 1.19 to 1.69 Å. Using this potential we obtain MXene that is mechanically stable without external loading force and gives ultimate strength of 11.36 GPa which is the same order or magnitude to experimental estimation from indentation measurements of (17.3±1.6 GPa).[39]

2.2 Modelling the bridged structure in ultrathin sheets

The interest of our study is on the bridged structures in a 2D graphene, MoS_2 and MXene (Ti_3C_2) sheet. We create different samples of these 2D sheets with varying architectures. We created samples with changing bridge height and changing bridge width. The bridged structure is generated using a custom python script by essentially deleting atoms from a 2D pristine sheet. We start out

with a pristine sheet of dimensions (l x b) and then use location data to delete the atoms in the shape of a rectangle for the defects and a notch defect at the edge to create the desired architecture. This might lead to hanging atoms with free ends at the edges of the bridged defects, but analysis showed that they did not contribute to the stress distribution in the ultrathin sample. These atoms were not involved in distributing the stress that occurs due to the uniaxial stretching of the sheets. In Fig. 1A which shows the schematic of a typical sample, l is the length of the sample of 510 Å, b is the width of the sample of 245 Å, h is the height of the bridges and d is the width of the bridges. We make a notch at one end to allow for crack propagation into the sample. It is of length denoted by a, which is set to 100 Å. The angle of the crack tip is taken to be 20 degrees. The green boxes show the atoms that are fixed to the wall to allow for the uniaxial tension tests and the arrows show the direction the sample is being strained.

Fig. 1(b) shows a sample of the graphene sheet used for the simulations. The inset shows a magnified version of the sample. It is a single layer material sheet. The direction for the strain is along the zigzag direction. The setup for MoS_2 which is a 3-layer material, is shown in Fig. 1C. It shows the Mo atoms sandwiched between two layers of S atoms. The direction of strain is again along the zigzag direction. A schematic of the structure and direction of strain is shown in the supplementary material (Fig S1(a)). In case of MXene, Ti_3C_2 without functional groups is the sample material which is five layered is shown in Fig. 1(d). It is an alternating layer of Ti and C atoms. The structure is illustrated in (Fig. S1(b)) the supplementary material. The inset in all cases shows the magnified view of the atoms.

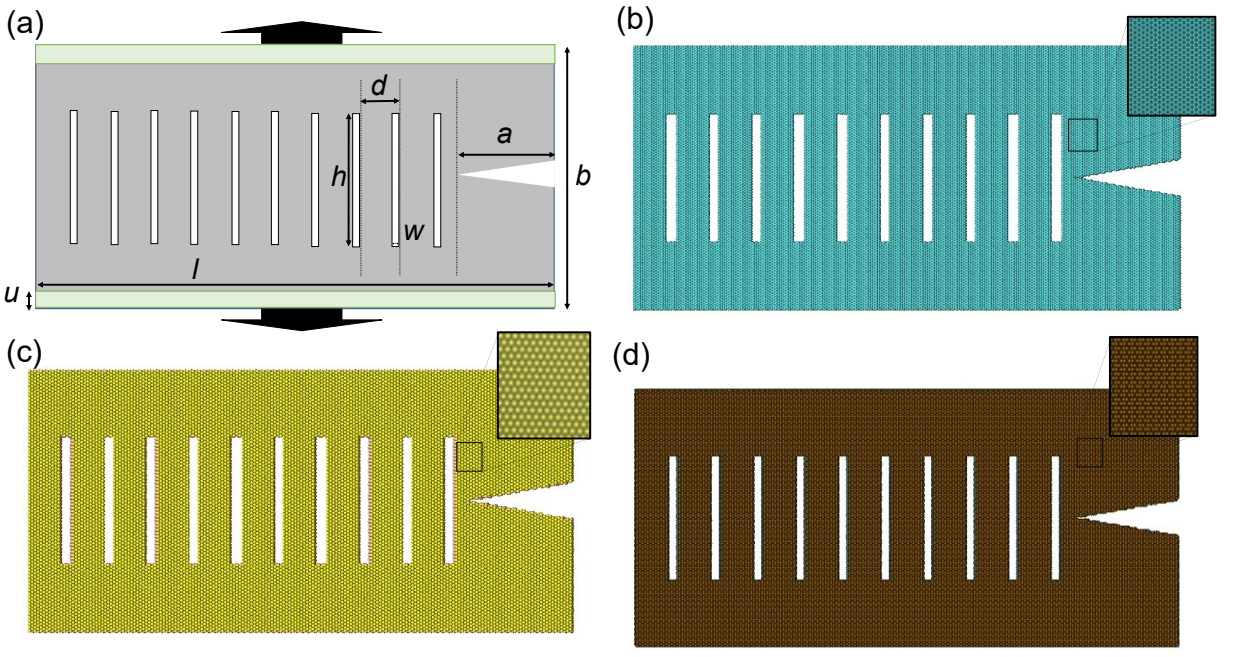

Figure 1. Schematics and atomistic structures of 2D material samples with bridge structure. The sheet is of length (l) and height (b), and the bridge structure is composed of gaps of height (h) in parallel and width (w) with a distance (d) between them and a pre-existing crack of length (a). We fix regions of the lower and upper boundaries of the sample (as highlighted by the green boxes of height (u)) and apply uniaxial tensile strain to the graphene sample by separating the two regions with a constant strain rate. The Fig. 1(b), 1(c) and 1(d) shows the samples of graphene, MoS_2 and MXene, respectively, with the inset showing a zoomed-in version.

There are 10 bridged defects in all the samples. We conduct studies by changing the height of the defects. The height of the bridges ranges from h =0 Å for the pristine case to h = 120 Å for the highest bridge. The width of the bridge, d = 30 Å, is kept constant along with the defect width, w = 10 Å while varying the height, h. We studied seven samples for each material with heights, h = (0 Å, 5 Å, 20 Å, 40 Å, 60 Å, 100 Å, 120 Å).

The boundary conditions are periodic, but care has been taken to make sure that the sample does not interact with itself from the image by making sure that the box is significantly larger than the sample. We keep 50 Å on both sides of the 2D sample and 20 Å in the thickness. So, the thickness dimension of the box ranges from -20 Å to 20 Å and the length of the box is -50 Å to 560 Å and the width is from -50 Å to 300 Å.

2.3 Relaxation before fracture simulation

The sheets are energetically minimized before fracturing. The system is minimized with conjugate gradient method for 20,000 steps with a timestep of 1fs. The system is then equilibrated using a NVE ensemble to a temperature of 300 K by rescaling the velocity of individual atoms with a timestep of 1 fs for 10000 steps for graphene, MoS_2 and MXene. The energy for equilibration is plotted and discussed to see if the material energy has reached a constant value in supplementary information(Fig. S2 and Fig. S3).

2.4 Fracture simulation and visualization

The sheet is stretched in the zigzag direction to generate the fracture mechanics. A few blocks of the upper and lower atoms in the zigzag direction denoted by the green boxes in Fig. 1(a) of dimension (u x l x t) where t is the thickness of the material, are fixed to the edge of the simulation box. The simulation box is then deformed along the zigzag direction with an engineering strain rate of 0.0000002Å/fs.[40] This rate is slow and is done in order to avoid overestimating the energy release rate [29]. This is done for 10 ns. However, the sheet is observed to facture way before the end of the simulation steps. The thickness of graphene is assumed to be 3.35 Angstroms [41] , for the MoS_2 it is 6.50 Å[42] and for the Ti_3C_2 it was 9.88 Å [43] . The atomic Virial is employed to calculate the atomistic stress of atom. This is color coded in the dynamics demonstration in Fig. 2, Fig.3 and Fig. 4 with the color scale. All our MD simulations are performed using LAMMPS [44]. We use VMD [45] to visualize the atomic structures, dynamics and stress distributions.

2.5 Post-simulation Analysis

The simulation results are outputted every 100 fs. The stress is computed as

$$\sigma = \frac{F_{top}}{(l \times t)} \tag{4}$$

where σ is the stress in the $\sigma - \epsilon$ plots in Fig. 2, Fig. 3 and Fig. 4. F_{top} is the force on the fixed set of atoms denoted by the green section of the atoms in Fig. 1(a), l is the length of the sample and t is the thickness of the sample.

The strain, ϵ is computed as

$$\epsilon = e_{rate} \times \Delta t \times n_{steps} \quad (5)$$

where e_{rate} is the strain rate of the simulation, Δt is the timestep of the simulation, and n_{steps} is the number of simulation steps. A brief analysis of the effect of defects with bridge width on the strength of the sample is shown in the supplementary information (Fig. S4). We also conducted a study with changing crack-tip position, orientation, and the density of bridges in the graphene sample. The results and a brief discussion are provided in supplementary information (Section S5)

3. Results

The $\sigma - \epsilon$ plot in Fig 2 (a) summarizes the stress strain relationship with changing height of the defects. The inset shows that as we increase the size of the defects the Young's modulus of the sample decreases. We also see that there is a decrease in ultimate stress of the material with defect size. As we increase the height of the defects we observe a subtle second loading curve with a second stress peak for bridge heights, h >= 5 Å which becomes more prominent with bridge height. In the dynamics which is showcased in the Fig. 2(b)-(d) we see the stress distribution with strain.

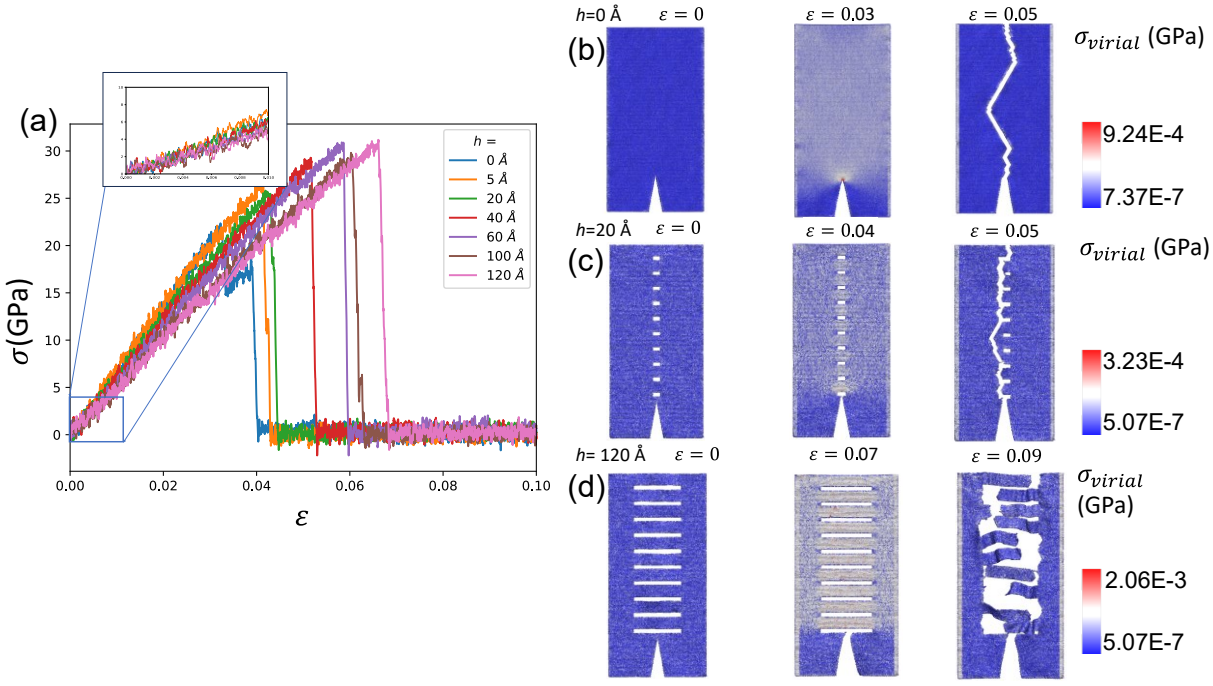

Figure 2. The stress-strain and stress dynamics of graphene sheet. (a) The stress strain of graphene with changing bridge height. The arrows indicate the relaxed state, the first stress drop and the second stress loading from left to right. (b) Dynamics and stress concentration of pristine graphene, h = 0 Å for three strain values. (c) Dynamics and stress concentration of small, bridged graphene, h = 20 Å for three strain values. (d) Dynamics and stress concentration of high bridged graphene, h = 120 Å for three strain values. It is shown that the crack propagation within the pristine graphene and graphene with short bridges (h = 0 Å and h = 20 Å) are similar, and long bridges (h = 120 Å) are dissipating the deformation energy by involving more atoms in deformation and preventing the propagation of crack at higher strain level (e.g., ε = 0.09). The inset in (a) shows that the material Young's modulus decreases with defects introduction.

For the pristine case Fig 2(b) we see that there is stress concentration at the crack tip at $\varepsilon = 0.03$. On increasing the strain this tip drives forward the crack propagation until the material fails. For small bridges, h=20 Å like in Fig 2(c) we once again see the stress concentration at the crack tip at $\varepsilon = 0.04$. The distribution of stress coincides with the corners of the bridges and hence on further strain we see the material fails without a significant second loading. The crack propagation is along the bridge corners which guide the material failure as can be seen for $\varepsilon = 0.05$. For larger bridge heights, like h = 120 Å as in Fig 2(c) we can see that once that crack tip fails the material is able to hinder the crack propagation for $\varepsilon = 0.07$ as the corners of the bridges are far away from the initial crack tip. This leads to a deformation of the bridges extensively with a second loading which happens because of the maximum amount of load being shared among the bridged structures now and with further strain the material fails with crack occurring along the corner of the bridges for $\varepsilon = 0.09$.

This leads to a brittle-ductile like transition for the material which is evident from the stress-strain plot in Fig 2(a).

We find a similar brittle-ductile transition trend for MoS_2 by increasing the h value (Fig. 3). It can again be seen that for the stress-strain curve in Fig. 3(a) there is a decrease in Young's modulus

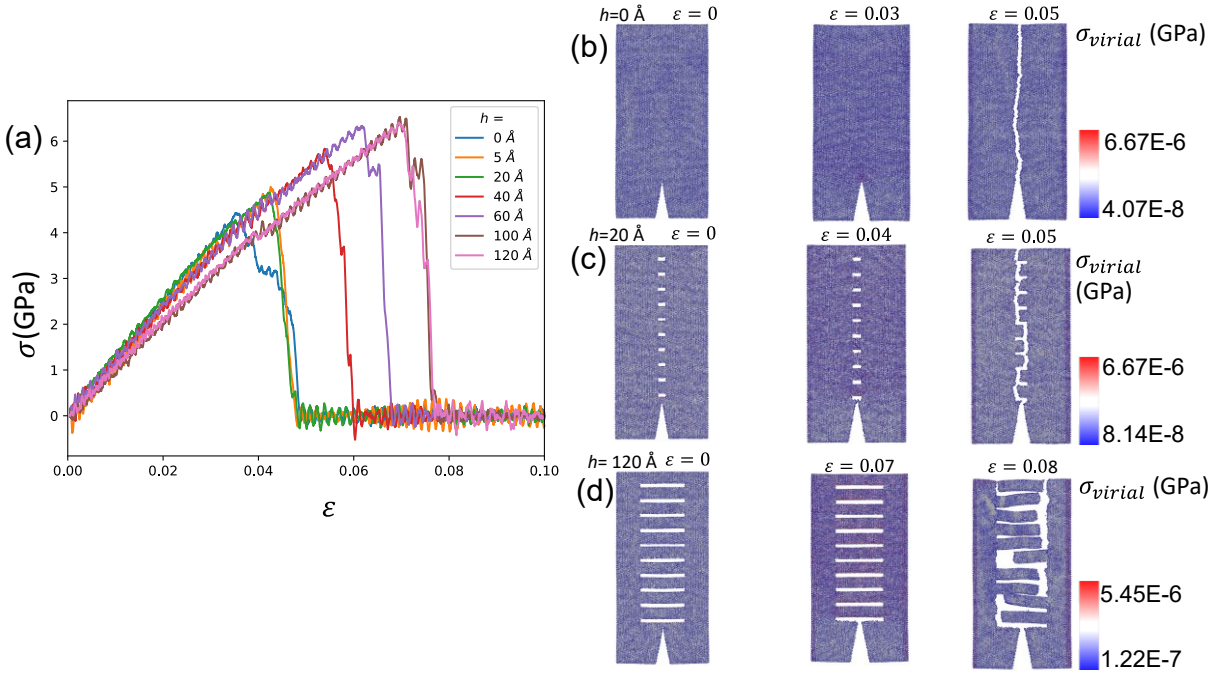

Figure 3: The stress-strain and stress dynamics of MoS_2 samples**.** (a) The stress strain of MoS_2 with changing bridge height. Moving average of 50 fs to minimize the noise in the stress-strain profile (b) Dynamics and stress concentration of pristine MoS_2, h = 0 Å for three strain values. (c) Dynamics and stress concentration of small bridged MoS_2, h = 5 Å for three strain values. (d) Dynamics and stress concentration of high bridged MoS_2, h = 60 Å for three strain values. The yield strain of the sample increases as the height of the defects increases. The bridges sustain most of the strain energy as can be seen for h = 60 Å at ε = 0.05.

for the increasing defect size for the material. We can also see that there are signs of secondary loading for h >= 40 Å. This is not as prominent as in the graphene case. It is shown that MoS_2, in

comparing to graphene, is more sensitive to h, as the cracked MoS_2 fractures with a lower ultimate stress than graphene. For h = 0 Å we see brittle failure in Fig. 3(b) with high stress concentration at the crack tip. The influence of stress concentration is also more localized than graphene. This is clear from the crack tip propagation which closely follows the center of the sample for $\varepsilon = 0.05$ in contrast to graphene where the crack tip moves much longer distance across the sample. For $h >$ 0 Å we see that the sample fails with crack propagating along the corner of the bridges, even for very short bridges. Fig. 3(c) and 3(d) show that the lower ultimate strain of MoS_2 limits the deformation of the bridges, making them less stretchable than graphene bridges, but still there is clear stress concentration in the bridges (Fig. 3(d)) at $\varepsilon = 0.05$ and therefore the sample is tougher than the pristine case. This is evident from Fig. 3(a) as there is no significant reduction in the energy dissipation (area below the stress-strain curves) as compared to graphene for small values of h <= 10 Å.

The σ-ϵ plots for MXene is summarized in Fig. 4(a) for various h. We see that the ultimate stress decreases with defect size. There is a significant decrease from 10 GPa for pristine case to 5 GPa for bridge with height, h = 120 Å. We also see that the material has a ductile failure as compared to the previous samples. We notice that the samples with larger defects fail at lower strain values of $\varepsilon = 0.2$ for the h = 120 Å as compared to $\varepsilon = 0.5$ for pristine case, h = 0 Å .The failure of MXene (Fig. 4(b)) suggests that it is ductile before introducing bridge defects, as shown by the shear band

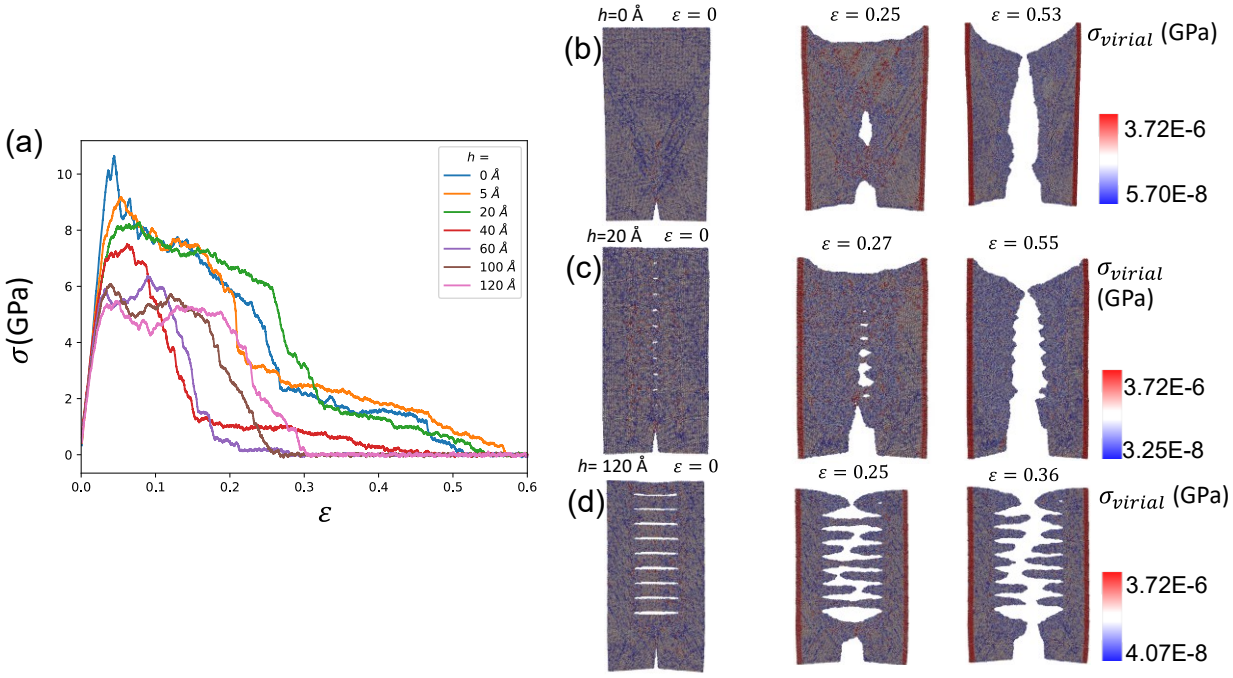

Figure 4. The stress-strain and stress dynamics of MXene, Ti_3C_2 samples. (a) The stress strain with changing bridge height. Moving average of 100 ps window to minimize the noise in the stress strain profile (b) Dynamics and stress concentration of pristine MXene, h = 0 Å for three strain values. (c) Dynamics and stress concentration of small bridged MXene, h = 20 Å for three strain values. (d) Dynamics and stress concentration of high bridged MXene, h = 120 Å for three strain values. There is a decrease in the ultimate strength of the sample with increasing bridge height in (a). The ductile nature of the sample with defect tolerance is clear from a secondary crack propagation from the center instead of the crack tip, panel (b), (c) and (d) for $\varepsilon = 0.25$, $\varepsilon = 0.27$ and $\varepsilon = 0.25$ respectively.

along the 45° in front of the crack tip and the strong necking behavior before material rupture (ε = 0.25, 0.53), making MXene very different from the previous two samples. Furthermore, it is shown that the material is not sensitive to defects since the crack does not spread from the tip of the crack (ε = 0.25). Instead, a daughter crack initiates from the center of where the ±45° shear bands meet and dominates the material failure. For short bridges h = 20 Å we can see in Fig. 4(c) that the defects far from the initial crack is healed for ε = 0.27 and stress is not concentrated at the bridge corners and the material opens at the bridge center and then propagates through for ε = 0.55. In the case of long bridges h = 120 Å we see in Fig. 4(d) that instead of the corners the material fails at the center of the bridges after 'thinning' of the bridges for ε = 0.25. There is no brittle to ductile transition and the sample is always ductile with heavy deformation as is clear from the healing of the defects by neighboring molecules.

4.Discussion

We summarize the toughness modulus of these cracked materials, by integrating the area under the stress strain curve, as a function of the bridge height in Figs. 5(a)-(c). These values reflect the energy release rate normalized by the same sample height (b). It is shown that for graphene (Fig. 5(a)) there is a rapid increase in dissipation energy which becomes with increasing defect size. Similar is the case with MoS_2 with steady increase shown in Fig. 5(b). For MXene, we see a slight increase and then a sharp decrease in the energy for Fig. 5(c).

4.1 Calculation of energy dissipation

We developed a mathematical model to better illustrate how the bridge dimensions contribute to energy dissipation in different 2D materials. We noticed that there are two mechanisms that account for the energy release during the fracture process. Firstly, the release of the deformation energy of the high-stress region after fracture and secondly the free surface (bond breaking) created during the fracture process, as illustrated in Fig. 5(d), while both the high-stress region and the total crack path length vary with the bridge dimensions. By considering the combination of both terms we can quantitatively explain the total energy release as a function of the 2D materials with bridge structures.

To estimate the deformation energy stored inside the bridged material before rupture, we generally consider the bridges as porous features, and the material stiffness and strength is given by the scaling law of open-cell porous materials (Gibson)

$$E = \left(\frac{\rho}{\rho_0}\right)^2 E_0 \tag{6}$$

$$\sigma_U = \left(\frac{\rho}{\rho_0}\right)^{1.5} \sigma_{U0} \tag{7}$$

where E, σ_U, ρ are the Young's modulus, ultimate strength and density of porous material, respectively. E_0, σ_{U0}, ρ_0 are the corresponding physical properties without pores. According to the geometry of the bridged 2D material, it is noted that for the sample

$$\frac{\rho}{\rho_0} = 1 - \frac{wh}{db} \tag{8}$$

Where h and d are the height and periodic width of the bridge structure, b is the total height of the sample and w is the width of each gap. Eq. (8) is essentially the effective density of the sample with the porous bridge structure (wh/db) subtracted from the total bridge $(db/db = 1)$.

The deformation in the bridges is given by Eq. (9). which is the effective density of the bridge structure

$$\frac{\rho}{\rho_0} = \left(\frac{h(d-w)}{db}\right) \tag{9}$$

By considering Eq. (6) ~ (9), the deformation energy denoted by the expression of the form $U_{def} = \frac{1}{2}\frac{\sigma^2}{E}$, that dominates small h can be computed by treating the defects as voids and is given by Eq. (10)

$$U_{1a} = \left(1 - \frac{wh}{db}\right)\frac{\sigma^2}{2E} \tag{10}$$

and the deformation energy that dominates large h can be computed by summing the energy of the highly deformed region between two neighboring bridges as in Eq. (11).

$$U_{1b} = \left(\frac{h(d-w)}{db}\right)\frac{\sigma^2}{2E} \tag{11}$$

From the schematics in Fig. 5(d) and Fig. 1(a) the energy release by considering the free surface during fracture, denoted by dotted red lines in Fig. 5(d) of the sample, for short bridges is given by Eq. (12)

$$U_{2a} = \frac{\gamma \int d\,l}{V} = \frac{\gamma L\left(1 + \frac{h}{d}\right)}{bLt} = \frac{\gamma\left(1 + \frac{h}{d}\right)}{bt} \tag{12}$$

For energy release in case of long bridges due to bond breaking is in Eq. (13)

$$U_{2b} = \frac{\gamma\left(1 - \frac{w}{d}\right)}{bt} \tag{13}$$

where γ with unit of energy/length is the surface energy of the 2D material, t is the thickness of the 2D material, V is the volume of the sample and dl is the length elements along the crack path. In Eq. (12) the length element contribution is shown in Fig. 5(d) for the smaller bridges which shows that the crack path is along the height of the bridges. Similarly, the contributions for the Eq. (13) is across the corners of the bridges.

The symbols have the same meaning as shown in Fig 1(a), and σ, E and γ are the ultimate stress, Young's modulus, and the surface energy of the 2D materials with units of energy per unit length, that are obtained from individual MD simulations with their numerical values summarized in the supplementary material (in Table S1 and Fig. S5). Combining these two equations using simple mixed mode we have the total energy release given by

$$\mathrm{U} = \left(1 - \frac{h}{b}\right)(\alpha U_{1a} + U_{2a}) + \left(\frac{h}{b}\right)(\beta U_{1b} + U_{2b}) \tag{14}$$

where for small h the crack propagation around the bridges dominates along with the deformation at crack tip whose strength is controlled by the parameter α. For large h, the crack propagation at the corner of the bridges is dominant along with the deformation of the bridges whose strength is controlled by parameter β.

We used this function to best fit the dissipation energy by determining the α and β values for each of the three materials. The numerical values are summarized in the supplemental information (Table S1) and the fitting results are summarized in Fig. 5 with the green dotted lines. For graphene we see that there is good agreement with rapid increase followed by a gradual increase in energy with increasing height. We observe a consistent rise in the dissipation energy for MoS_2, which is attributed to its high brittleness and low flexibility, resulting from a lower ratio of ultimate strength to Young's modulus as compared to graphene. On the other hand, in MXene, we observe a slight increase in energy for small h, followed by a steady decrease, but there is a lack of good agreement for large h in this case. This could be attributed to the highly ductile and defect-resistant nature of MXene, which makes it challenging to accurately predict the volume of deformation and propagation of crack surfaces. Details about the parameters and values are provided in the supplemental information (Fig. S5 and Table S1).

Hence, we see that for brittle materials, like graphene and MoS_2, it is favorable to have bridge defects with larger h as it increases the strength of the material with its second loading mechanism. Smaller bridge heights, $h \sim 5$ Å, as seen in graphene can lead to lower material strength due to the interaction between the stress concentrations at crack tip and bridge corners. For a less stretchable material like MoS_2 this effect is less pronounced for smaller defects and bridges with smaller heights can also increase material strength. For a ductile material like MXene, we see that having smaller or no defects is best for material strength. Larger defects effectively reduce the material

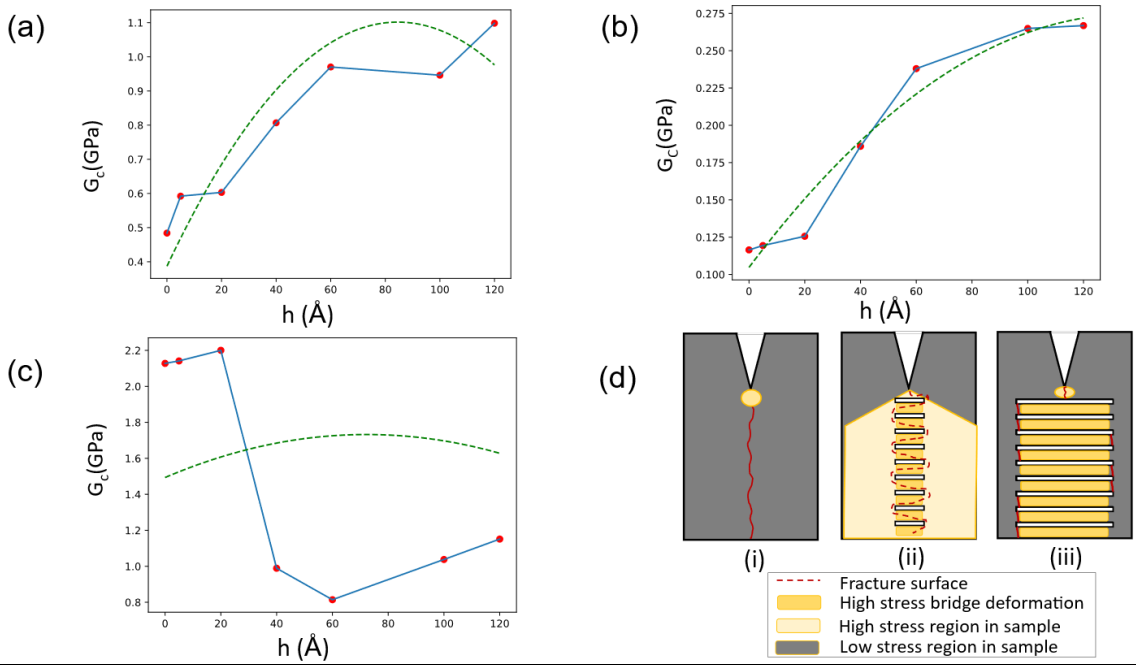

Figure 5. The dissipation energy (solid line is the simulation result and dashed green lines are for the theoretical prediction with fitted parameters) with changing bridge height and material mechanics. (a) is for graphene sample. (b) is for MoS2 and (c) is for MXene. (d) Three ways for energy dissipation. (i) is for pristine materials ($h = 0$ Å) where there is bond breaking denoted by red dotted lines and the deformation of the entire sample denoted by the yellow color. (ii) is for small h, there is propagation of crack around the bridges and there is deformation of the bridges denoted by yellow. (iii) is for large h, the bond breaking is at the corners of the bridge and there is deformation energy is primarily stored in the long bridges

integrity and its ultimate strength. This is the opposite to the effects on ductile materials. Therefore, we see that the design of these bridge-like defects needs to be catered according to the material properties.

5.Conclusion

Our study employs full atomistic simulations to investigate the fracture mechanics of ultrathin architected sheets of graphene, monolayer MoS_2, and MXene under uniaxial tensile strain. Our findings demonstrate that the incorporation of bridged defects can enhance the toughness of these samples compared to the pristine counterparts, in most cases. Notably, for brittle materials such as graphene and MoS_2, the increase in toughness can be as high as 50%. However, for ductile materials like MXene, this trend is not observed due to its high ductility and low sensitivity to defects.

We also developed a theoretical model to predict the energy dissipation based on material deformation and surface crack propagation. Our findings indicate that for small-height defects, surface crack propagation contributes more to the energy dissipation, while the overall sample deformation plays a smaller role. As the height of the bridges increases, the deformation in the long bridges allows for a larger portion of the sample to dissipate strain energy, which dominates over crack propagation. Specifically, we observe a steady decrease followed by an increase in energy dissipation with increasing defect height for highly flexible graphene samples. However, for MoS_2, we see a more aggressive increase in material strength due to its low Young's modulus and deformation. In contrast, for MXene, we observe a slight increase for small defects followed by a sudden decrease due to the sample's ductility. These trends demonstrate the applicability of the theoretical predictions to the various samples.

Previous studies have focused on reinforcing 2D materials such as graphene, MoS_2, and MXene by introducing point defects and composite materials to improve their mechanical strength. However, our current study demonstrates that the incorporation of architected defects alone can enhance the strength of these highly versatile ultrathin materials. These simulations and theoretical analyses provide a foundation for fabricating stronger 2D materials. While fabricating these defects remains a challenging task, our findings serve as further experimental motivation for the fabrication and testing of these novel architected materials for various applications.

ASSOCIATED CONTENT

Supporting Information. The following files are available free of charge. The material preparation and simulation parameters (file type DOC)

Corresponding Author

*Zhao Qin: zqin02@syr.edu

Author Contributions

Z.Q. proposed and designed the research. Z.Q. and C.Y. supervised the research work. K.P. and Z.Q. prepared the computational model and analyzed the results. K.P and C.Z. performed the MD simulations. K.P. and Z.Q. lead the manuscript writing and all authors revised and approved the manuscript.

ACKNOWLEDGMENT

Z.Q. acknowledge the National Science Foundation CAREER Grant (Award #: 2145392), the startup funding and Collaboration for Unprecedented Success and Excellence (CUSE) Grant at Syracuse University for supporting the research work.

References

(1) Castro Neto, A. H.; Guinea, F.; Peres, N. M. R.; Novoselov, K. S.; Geim, A. K. The Electronic Properties of Graphene. *Rev. Mod. Phys.* **2009**, *81* (1), 109–162. https://doi.org/10.1103/RevModPhys.81.109.

(2) Cheng, Y.; Zhou, S.; Hu, P.; Zhao, G.; Li, Y.; Zhang, X.; Han, W. Enhanced Mechanical, Thermal, and Electric Properties of Graphene Aerogels via Supercritical Ethanol Drying and High-Temperature Thermal Reduction. *Sci Rep* **2017**, *7* (1), 1439. https://doi.org/10.1038/s41598-017-01601-x.

(3) Jung, G.; Qin, Z.; Buehler, M. J. Molecular Mechanics of Polycrystalline Graphene with Enhanced Fracture Toughness. *Extreme Mechanics Letters* **2015**, *2*, 52–59. https://doi.org/10.1016/j.eml.2015.01.007.

(4) Balandin, A. A.; Ghosh, S.; Bao, W.; Calizo, I.; Teweldebrhan, D.; Miao, F.; Lau, C. N. Superior Thermal Conductivity of Single-Layer Graphene. *Nano Lett.* **2008**, *8* (3), 902–907. https://doi.org/10.1021/nl0731872.

(5) Lee, C.; Wei, X.; Kysar, J. W.; Hone, J. Measurement of the Elastic Properties and Intrinsic Strength of Monolayer Graphene. *Science* **2008**, *321* (5887), 385–388. https://doi.org/10.1126/science.1157996.

(6) *The rise of graphene | Nature Materials*. https://www.nature.com/articles/nmat1849 (accessed 2022-12-20).

(7) Novoselov, K. S.; Geim, A. K.; Morozov, S. V.; Jiang, D.; Katsnelson, M. I.; Grigorieva, I. V.; Dubonos, S. V.; Firsov, A. A. Two-Dimensional Gas of Massless Dirac Fermions in Graphene. *Nature* **2005**, *438* (7065), 197–200. https://doi.org/10.1038/nature04233.
(8) Bertolazzi, S.; Brivio, J.; Kis, A. Stretching and Breaking of Ultrathin MoS_2. *ACS Nano* **2011**, *5* (12), 9703–9709. https://doi.org/10.1021/nn203879f.
(9) Yang, K.; Liu, T.; Zhang, X.-D. Bandgap Engineering and Near-Infrared-II Optical Properties of Monolayer MoS2: A First-Principle Study. *Frontiers in Chemistry* **2021**, *9*.
(10) Zahedi, R.; Alajlan, N.; Zahedi, H.; Rabczuk, T. Mechanical Properties of All MoS_2 Monolayer Heterostructures: Crack Propagation and Existing Notch Study. *cmc* **2021**, *70* (3), 4635–4655. https://doi.org/10.32604/cmc.2022.017682.
(11) Yan, R.; Simpson, J. R.; Bertolazzi, S.; Brivio, J.; Watson, M.; Wu, X.; Kis, A.; Luo, T.; Hight Walker, A. R.; Xing, H. G. Thermal Conductivity of Monolayer Molybdenum Disulfide Obtained from Temperature-Dependent Raman Spectroscopy. *ACS Nano* **2014**, *8* (1), 986–993. https://doi.org/10.1021/nn405826k.
(12) Gogotsi, Y.; Anasori, B. The Rise of MXenes. *ACS Nano* **2019**, *13* (8), 8491–8494. https://doi.org/10.1021/acsnano.9b06394.
(13) Lipatov, A.; Goad, A.; Loes, M. J.; Vorobeva, N. S.; Abourahma, J.; Gogotsi, Y.; Sinitskii, A. High Electrical Conductivity and Breakdown Current Density of Individual Monolayer Ti3C2Tx MXene Flakes. *Matter* **2021**, *4* (4), 1413–1427. https://doi.org/10.1016/j.matt.2021.01.021.
(14) Chen, H.; Wen, Y.; Qi, Y.; Zhao, Q.; Qu, L.; Li, C. Pristine Titanium Carbide MXene Films with Environmentally Stable Conductivity and Superior Mechanical Strength. *Advanced Functional Materials* **2020**, *30* (5), 1906996. https://doi.org/10.1002/adfm.201906996.
(15) Ibrahim, Y.; Mohamed, A.; Abdelgawad, A. M.; Eid, K.; Abdullah, A. M.; Elzatahry, A. The Recent Advances in the Mechanical Properties of Self-Standing Two-Dimensional MXene-Based Nanostructures: Deep Insights into the Supercapacitor. *Nanomaterials* **2020**, *10* (10), 1916. https://doi.org/10.3390/nano10101916.
(16) Liu, R.; Li, W. High-Thermal-Stability and High-Thermal-Conductivity $Ti_3C_2T_x$ MXene/Poly(Vinyl Alcohol) (PVA) Composites. *ACS Omega* **2018**, *3* (3), 2609–2617. https://doi.org/10.1021/acsomega.7b02001.
(17) Wang, J.; Shen, M.; Liu, Z.; Wang, W. MXene Materials for Advanced Thermal Management and Thermal Energy Utilization. *Nano Energy* **2022**, *97*, 107177. https://doi.org/10.1016/j.nanoen.2022.107177.
(18) Wang, G.; Wang, Y.-P.; Li, S.; Yang, Q.; Li, D.; Pantelides, S. T.; Lin, J. Engineering the Crack Structure and Fracture Behavior in Monolayer MoS2 By Selective Creation of Point Defects. *Advanced Science* **2022**, *9* (22), 2200700. https://doi.org/10.1002/advs.202200700.
(19) Fatima, M.; Fatheema, J.; Monir, N. B.; Siddique, A. H.; Khan, B.; Islam, A.; Akinwande, D.; Rizwan, S. Nb-Doped MXene With Enhanced Energy Storage Capacity and Stability. *Frontiers in Chemistry* **2020**, *8*.
(20) Wan, S.; Li, X.; Chen, Y.; Liu, N.; Du, Y.; Dou, S.; Jiang, L.; Cheng, Q. High-Strength Scalable MXene Films through Bridging-Induced Densification. *Science* **2021**, *374* (6563), 96–99. https://doi.org/10.1126/science.abg2026.
(21) Hacopian, E. F.; Yang, Y.; Ni, B.; Li, Y.; Li, X.; Chen, Q.; Guo, H.; Tour, J. M.; Gao, H.; Lou, J. Toughening Graphene by Integrating Carbon Nanotubes. *ACS Nano* **2018**, *12* (8), 7901–7910. https://doi.org/10.1021/acsnano.8b02311.

(22) Hanakata, P. Z.; Cubuk, E. D.; Campbell, D. K.; Park, H. S. Accelerated Search and Design of Stretchable Graphene Kirigami Using Machine Learning. *Phys. Rev. Lett.* **2018**, *121* (25), 255304. https://doi.org/10.1103/PhysRevLett.121.255304.
(23) Blees, M. K.; Barnard, A. W.; Rose, P. A.; Roberts, S. P.; McGill, K. L.; Huang, P. Y.; Ruyack, A. R.; Kevek, J. W.; Kobrin, B.; Muller, D. A.; McEuen, P. L. Graphene Kirigami. *Nature* **2015**, *524* (7564), 204–207. https://doi.org/10.1038/nature14588.
(24) Zhang, T.; Li, X.; Gao, H. Designing Graphene Structures with Controlled Distributions of Topological Defects: A Case Study of Toughness Enhancement in Graphene Ruga. *Extreme Mechanics Letters* **2014**, *1*, 3–8. https://doi.org/10.1016/j.eml.2014.12.007.
(25) Heide-Jørgensen, S.; Budzik, M. K.; Turner, K. T. Mechanics and Fracture of Structured Pillar Interfaces. *Journal of the Mechanics and Physics of Solids* **2020**, *137*, 103825. https://doi.org/10.1016/j.jmps.2019.103825.
(26) Wang, S.; Qin, Z.; Jung, G. S.; Martin-Martinez, F. J.; Zhang, K.; Buehler, M. J.; Warner, J. H. Atomically Sharp Crack Tips in Monolayer MoS2 and Their Enhanced Toughness by Vacancy Defects. *ACS Nano* **2016**, *10* (11), 9831–9839. https://doi.org/10.1021/acsnano.6b05435.
(27) Stuart, S. J.; Tutein, A. B.; Harrison, J. A. A Reactive Potential for Hydrocarbons with Intermolecular Interactions. *J. Chem. Phys.* **2000**, *112* (14), 6472–6486. https://doi.org/10.1063/1.481208.
(28) Kim, Y.-M.; Lee, B.-J. Modified Embedded-Atom Method Interatomic Potentials for the Ti–C and Ti–N Binary Systems. *Acta Materialia* **2008**, *56* (14), 3481–3489. https://doi.org/10.1016/j.actamat.2008.03.027.
(29) Zhang, Z.; Wang, X.; Lee, J. D. An Atomistic Methodology of Energy Release Rate for Graphene at Nanoscale. *Journal of Applied Physics* **2014**, *115* (11), 114314. https://doi.org/10.1063/1.4869207.
(30) Buehler, M. J.; Keten, S. Colloquium: Failure of Molecules, Bones, and the Earth Itself. *Rev. Mod. Phys.* **2010**, *82* (2), 1459–1487. https://doi.org/10.1103/RevModPhys.82.1459.
(31) Brenner, D. W. Empirical Potential for Hydrocarbons for Use in Simulating the Chemical Vapor Deposition of Diamond Films. *Phys. Rev. B* **1990**, *42* (15), 9458–9471. https://doi.org/10.1103/PhysRevB.42.9458.
(32) Shenderova, O. A.; Brenner, D. W.; Omeltchenko, A.; Su, X.; Yang, L. H. Atomistic Modeling of the Fracture of Polycrystalline Diamond. *Phys. Rev. B* **2000**, *61* (6), 3877–3888. https://doi.org/10.1103/PhysRevB.61.3877.
(33) Qin, Z.; Zou, J.; Yin, Y.; Yu, S.-W. Superior Flexibility of Super Carbon Nanotubes: Molecular Dynamics Simulations. *Applied Physics Letters* **2007**, *91*, 043108–043108. https://doi.org/10.1063/1.2760039.
(34) Sammalkorpi, M.; Krasheninnikov, A.; Kuronen, A.; Nordlund, K.; Kaski, K. Mechanical Properties of Carbon Nanotubes with Vacancies and Related Defects. *Phys. Rev. B* **2004**, *70* (24), 245416. https://doi.org/10.1103/PhysRevB.70.245416.
(35) Yeo, J.; Jung, G. S.; Martín-Martínez, F. J.; Beem, J.; Qin, Z.; Buehler, M. J. Multiscale Design of Graphyne-Based Materials for High-Performance Separation Membranes. *Advanced Materials* **2019**, *31* (42), 1805665. https://doi.org/10.1002/adma.201805665.
(36) Wei, Y.; Wu, J.; Yin, H.; Shi, X.; Yang, R.; Dresselhaus, M. The Nature of Strength Enhancement and Weakening by Pentagon-Heptagon Defects in Graphene. *Nat Mater* **2012**, *11* (9), 759–763. https://doi.org/10.1038/nmat3370.

(37) Zhao, H.; Min, K.; Aluru, N. R. Size and Chirality Dependent Elastic Properties of Graphene Nanoribbons under Uniaxial Tension. *Nano Lett.* **2009**, *9* (8), 3012–3015. https://doi.org/10.1021/nl901448z.
(38) Stewart, J. A.; Spearot, D. E. Atomistic Simulations of Nanoindentation on the Basal Plane of Crystalline Molybdenum Disulfide (MoS2). *Modelling Simul. Mater. Sci. Eng.* **2013**, *21* (4), 045003. https://doi.org/10.1088/0965-0393/21/4/045003.
(39) Lipatov, A.; Lu, H.; Alhabeb, M.; Anasori, B.; Gruverman, A.; Gogotsi, Y.; Sinitskii, A. Elastic Properties of 2D Ti3C2Tx MXene Monolayers and Bilayers. *Science Advances* **2018**, *4* (6), eaat0491. https://doi.org/10.1126/sciadv.aat0491.
(40) Jung, G. S.; Irle, S.; Sumpter, B. G. Dynamic Aspects of Graphene Deformation and Fracture from Approximate Density Functional Theory. *Carbon* **2022**, *190*, 183–193. https://doi.org/10.1016/j.carbon.2022.01.002.
(41) Baskin, Y.; Meyer, L. Lattice Constants of Graphite at Low Temperatures. *Phys. Rev.* **1955**, *100* (2), 544–544. https://doi.org/10.1103/PhysRev.100.544.
(42) Zhao, Y.; Ouyang, G. Thickness-Dependent Photoelectric Properties of MoS2/Si Heterostructure Solar Cells. *Sci Rep* **2019**, *9* (1), 17381. https://doi.org/10.1038/s41598-019-53936-2.
(43) Tian, S.; Zhou, K.; Huang, C.-Q.; Qian, C.; Gao, Z.; Liu, Y. Investigation and Understanding of the Mechanical Properties of MXene by High-Throughput Computations and Interpretable Machine Learning. *Extreme Mechanics Letters* **2022**, *57*, 101921. https://doi.org/10.1016/j.eml.2022.101921.
(44) Plimpton, S. Fast Parallel Algorithms for Short-Range Molecular Dynamics. *Journal of Computational Physics* **1995**, *117* (1), 1–19. https://doi.org/10.1006/jcph.1995.1039.
(45) Humphrey, W.; Dalke, A.; Schulten, K. VMD: Visual Molecular Dynamics. *Journal of Molecular Graphics* **1996**, *14* (1), 33–38. https://doi.org/10.1016/0263-7855(96)00018-5.